AIAA JOURNAL
Vol. 49, No. 8, August 2011

Modeling Progressive Failure of Bonded Joints Using a Single Joint Finite Element

Scott E. Stapleton* and Anthony M. Waas†
University of Michigan, Ann Arbor, Michigan 48109
and
Brett A. Bednarcyk‡
NASA John H. Glenn Research Center at Lewis Field, Cleveland, Ohio 44135

DOI: 10.2514/1.J050889

Enhanced finite elements are elements with an embedded analytical solution that can capture detailed local fields, enabling more efficient, mesh-independent finite element analysis. In the present study, an enhanced finite element, referred to as a bonded joint element, that is capable of modeling an array of joint types is developed. The joint field equations are derived using the principle of minimum potential energy, and the resulting solutions for the displacement fields are used to generate shape functions and a stiffness matrix for a single joint finite element. This single finite element thus captures the detailed stress and strain fields within the bonded joint, but it can function within a broader structural finite element model. The costs associated with a fine mesh of the joint can thus be avoided, while still obtaining a detailed solution for the joint. Additionally, the capability to model nonlinear adhesive constitutive behavior has been included within the method, and progressive failure of the adhesive can be modeled by using a strain-based failure criteria and resizing the joint as the adhesive fails. Results of the model compare favorably with available experimental and finite element results.

I. Introduction

IN THE aerospace industry, fiber reinforced polymer matrix composites (FRPCs) are gaining increasing use and attention, because of their high strength-to-weight ratios, among other factors. FRPC joints perform much better with adhesive bonding rather than bolting or riveting, because of their quasi-brittle nature [1] and the ability of the bond to spread the load over a larger area, leading to a lessening of the stress concentration [2]. Therefore, accurate analysis of adhesively bonded joints is becoming more critical than ever.

Adhesive joints have traditionally been analyzed using two methods: analytical models and finite element analysis [3]. Analytical methods have been used to extract efficient closed-form solutions for adhesive single lap joint stresses. Classical formulas have been introduced by Volkerson [4], Goland and Reissner [5], Ojalvo and Eidinoff [6], and Hart-Smith [7]. More recently, refined analytical studies, carried out by Mortensen and Thomsen [8], Zhang et al. [9], and Delale et al. [10], have proven to be quite accurate in predicting stresses within adhesive joints. However, analytical methods are often limited by geometric assumptions used to obtain a closed-form solution and are not as useful to designers for compiling vehicle-scale models that may contain multiple joints. Finite element analyses are widely used in industry and can be used to assess joints with a wide variety of geometries and loading conditions. However, these methods can suffer from mesh dependence and a lack of efficiency, which is especially crippling for initial sizing analysis and full vehicle-scale models [11]. Therefore, a need exists to develop predictive tools for bonded joints that can be seamlessly coupled with large-scale structural analyses without adding major computational costs. Such tools can be used to make quick mesh-independent assessments of bonded composite joints. Currently, such a capability is lacking, and joint assessment is typically performed late in the design cycle when structural changes that can reduce weight are difficult and expensive to implement.

Gustafson and Waas [3] have merged analytical and finite element methods, in order to perform efficient, mesh-independent finite element analysis of double lap joints to use for initial design and macroscopic vehicle modeling. Analytical models were embedded into a single finite element with minimal analyst input. Stapleton and Waas [12] extended this method to single lap joints (Fig. 1), which are more complex due to the eccentricity of the axial load path. This eccentricity requires a careful consideration of the inclusion of nonlinear geometric effects if the joint rotations are sufficiently large, although these effects were not considered in the current model because rotations of the joints considered were small. The current study extends the method to include a nonlinear constitutive model for the adhesive in conjunction with inputs to cohesive zone finite element modeling [13,14] or a curve-fit to experimental test data. Additionally, a strain-based failure criterion is used to track damage in the adhesive and the joint element, and adjacent beam elements are resized to account for the failed adhesive. The entire joint can then be replaced by a single joint finite element, whereas the remaining structure (outside the joint) is modeled using standard structural elements, for instance beam elements (Fig. 1). As a result, failure in the adhesive is built into the joint element.

II. Analytical Formulation

The joint element with adhesive failure capabilities is an extension of the linear elastic joint element derived elsewhere (Stapleton and Waas [12]). The main difference is that this model now has the capability of handling adhesives with nonlinear constitutive behavior and has a failure criterion implemented within the model. A flow chart of the joint element implementation is shown in Fig. 2.

The individual steps will be expanded upon in the following sections, but the basic layout consists of first solving the linear problem to obtain shape functions, then defining a nonlinear stress–strain relation for the adhesive and linearizing this relation at each load increment. Following these steps, the joint stiffness matrix and

Presented as Paper 2010-3100 at the AIAA Structures, Structural Dynamics, and Materials Meeting, Orlando, FL, 12–15 April 2010; received 28 September 2010; revision received 3 March 2011; accepted for publication 27 March 2011.

*Graduate Student Research Assistant, Department of Aerospace Engineering; sstaple@umich.edu.
†Professor, Department of Aerospace Engineering; dcw@umich.edu. Associate Fellow AIAA.
‡Material Research Engineer, 21000 Brookpark Road; Brett.A.Bednarcyk@NASA.gov. Senior Member AIAA.

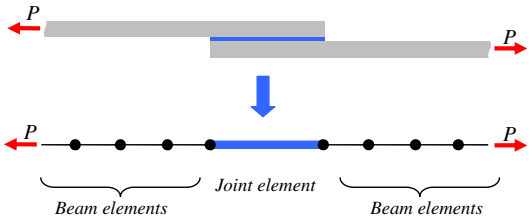

Fig. 1 The present study replaces a complex single lap joint mesh with a single joint element.

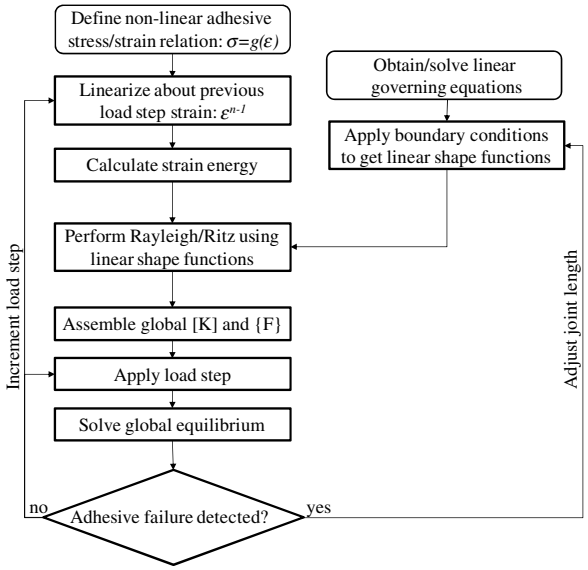

Fig. 2 Flow chart of the joint element with adhesive progressive failure.

force vector are calculated using the linear shape functions and strain energy for the nonlinear case. Finally, the global system is assembled, and the resulting equations are solved. Furthermore, the adhesive is checked for failure, and, in the case of adhesive failure, the length of the joint element decreases to account for failed adhesive.

A. Obtain Linear Shape Functions

To model nonlinear adhesive in a joint element, the shape functions are obtained from the case of a joint with a linear adhesive. To do this, the adhesive and adherends were assumed to be linearly elastic. Figure 3 illustrates the required geometric parameters and material properties of a single lap joint. The width of the joint in the y-direction is b. The subscripts 1, 2, and a denote variables associated with adherends 1, 2, and the adhesive, respectively.

Assuming the adherends behave like Euler–Bernoulli beams, the strain energy of the joint U is written as

$$U_{\text{joint}} = \frac{1}{2}\int_{V_1} \sigma_{1x}\varepsilon_{1x}\,\mathrm{d}V + \frac{1}{2}\int_{V_2} \sigma_{2x}\varepsilon_{2x}\,\mathrm{d}V + \frac{1}{2}\int_{V_a} (\sigma_{az}\varepsilon_{az} + \tau_{axz}\gamma_{axz})\,\mathrm{d}V \tag{1}$$

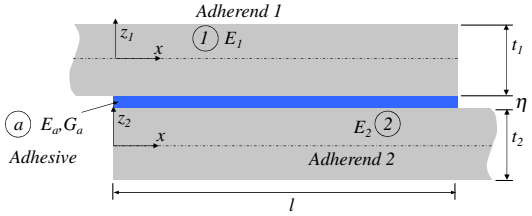

Fig. 3 Required geometric and material parameters for overlap region of a single lap joint.

in which σ_{ix} and ε_{ix} represent the normal stress and strain in material i (1 or 2 for the adherends) in the x-direction, σ_{az} and ε_{az} are the normal stresses/strains in the adhesive in the z-direction, τ_{azx} and γ_{azx} represent the shear stress–strain in the adhesive on the xz-plane, and all integrals are taken over the volume V_i of material i.

The two adherends are assumed to behave as beams, and the strain energy of the adherends can be found using standard Euler–Bernoulli beam theory. The derivation is not shown here, but the details are contained in Stapleton and Waas [12].

It should be noted that many adhesive joints involving bonded FRPCs are made up of thin adherends, which are relatively long in the y-direction, causing them to behave more like plates in cylindrical bending rather than beams. Though not done here, to model the adherends as wide plates in cylindrical bending, it is only a simple matter of replacing the modulus of elasticity E_i with $E_i/(1-\nu_i^2)$, $i = 1, 2$ and modeling the adhesive using plane strain, rather than plane stress assumptions. For joints that cannot accurately be modeled as beams or wide plates in cylindrical bending, it is important to also capture the displacements and stresses as a function of y (along the width of the joint). Future work will attempt to capture these effects, by making a plate type element.

A diagram of the notation scheme for the adhesive is shown in Fig. 4. It is assumed that the displacement varies linearly in the z_a-direction and that the adhesive and adherend are perfectly bonded at the interface. The displacements at the interface will be denoted by the subscripts in_1 and in_2.

The adhesive is modeled as a bed of linear normal and shear springs. In terms of the interface displacements, the strains in the adhesive are

$$\varepsilon_{az} = \frac{1}{\eta}(w_{\text{in}_1}(x) - w_{\text{in}_2}(x)) \tag{2a}$$

and

$$\gamma_{axz} = \frac{1}{\eta}(u_{\text{in}_1}(x) - u_{\text{in}_2}(x)) \tag{2b}$$

and the stresses are

$$\sigma_{az} = E_a\varepsilon_{az} \tag{3a}$$

and

$$\tau_{axz} = G_a\gamma_{axz} \tag{3b}$$

The interface displacements are defined in terms of adherend centerline displacements, using Euler–Bernoulli beam theory:

$$u_{\text{in}_1}(x) = u_1(x) + \frac{t_1}{2}\frac{\mathrm{d}w_1(x)}{\mathrm{d}x}, \qquad u_{\text{in}_2}(x) = u_2(x) - \frac{t_2}{2}\frac{\mathrm{d}w_2(x)}{\mathrm{d}x}$$
$$w_{\text{in}_1}(x) = w_1(x), \quad \text{and} \quad w_{\text{in}_2}(x) = w_2(x) \tag{4}$$

Using the principle of stationarity of potential energy, four fully coupled governing equilibrium differential equations are obtained from the energy expression in Eq. (1). Of the four governing equations, two correspond to the axial equilibrium, whereas two equations correspond to the transverse equilibrium. The axial

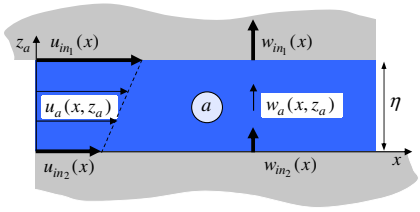

Fig. 4 Geometric and material parameters for overlap region of a single lap joint.

displacement equilibrium equations contain second-order derivatives, whereas the transverse displacement equations have fourth-order derivatives. The order of these equations can be reduced and assembled into a system of first-order constant coefficient homogeneous ordinary differential equations of the form

$$\{u\}_{,x} = [A]\{u\} \tag{5}$$

in which

$$\{u\} = [\,u_1 \quad u_{1,x} \quad w_1 \quad w_{1,x} \quad w_{1,xx} \quad w_{1,xxx} \quad u_2 \quad u_{2,x} \quad w_2 \quad w_{2,x} \quad w_{2,xx} \quad w_{2,xxx}\,] \tag{6}$$

and

$$[A] = \begin{bmatrix}
0 & 1 & 0 & 0 & 0 & 0 & 0 & 0 & 0 & 0 & 0 & 0 \\
\lambda_1 & 0 & 0 & \frac{1}{2}t_1\lambda_1 & 0 & 0 & -\lambda_1 & 0 & 0 & \frac{1}{2}t_2\lambda_1 & 0 & 0 \\
0 & 0 & 0 & 1 & 0 & 0 & 0 & 0 & 0 & 0 & 0 & 0 \\
0 & 0 & 0 & 0 & 1 & 0 & 0 & 0 & 0 & 0 & 0 & 0 \\
0 & 0 & 0 & 0 & 0 & 1 & 0 & 0 & 0 & 0 & 0 & 0 \\
0 & \frac{1}{2}t_1\Lambda_1 & -\Omega_1 & 0 & \frac{1}{4}t_1^2\Lambda_1 & 0 & 0 & -\frac{1}{2}t_1\Lambda_1 & \Omega_1 & 0 & \frac{1}{4}t_1\Lambda_1 t_2 & 0 \\
0 & 0 & 0 & 0 & 0 & 0 & 0 & 1 & 0 & 0 & 0 & 0 \\
-\lambda_2 & 0 & 0 & -\frac{1}{2}t_1\lambda_2 & 0 & 0 & \lambda_2 & 0 & 0 & -\frac{1}{2}t_2\lambda_2 & 0 & 0 \\
0 & 0 & 0 & 0 & 0 & 0 & 0 & 0 & 0 & 1 & 0 & 0 \\
0 & 0 & 0 & 0 & 0 & 0 & 0 & 0 & 0 & 0 & 1 & 0 \\
0 & 0 & 0 & 0 & 0 & 0 & 0 & 0 & 0 & 0 & 0 & 1 \\
0 & \frac{1}{2}t_2\Lambda_2 & \Omega_2 & 0 & \frac{1}{4}t_2\Lambda_2 t_1 & 0 & 0 & -\frac{1}{2}t_2\Lambda_2 & -\Omega_2 & 0 & \frac{1}{4}t_2^2\Lambda_2 & 0
\end{bmatrix} \tag{7}$$

with

$$\lambda_i = \frac{G_a b}{\eta E A_i}, \qquad i = 1, 2 \tag{8}$$

$$\Lambda_i = \frac{G_a b}{\eta E I_i}, \qquad i = 1, 2 \tag{9}$$

$$\Omega_i = \frac{E_a b}{\eta E I_i}, \qquad i = 1, 2 \tag{10}$$

Inspecting the matrix $[A]$ can be helpful in determining the nature of the solution and determining the solution method. There are 12 eigenvalues of $[A]$: two real eigenvalues, four complex eigenvalues, and six repeating eigenvalues. Therefore, the solution is made up of two exponential terms, four exponential terms multiplied by a sine or cosine, and the six repeating eigenvalues correspond to a third-order polynomial found in a standard beam solution. Such a complex solution shows that merely employing standard beam shape functions to the joint problem would be inadequate in capturing the nature of the whole solution.

The system in Eq. (5) can be solved using various methods, but calculating the matrix exponential [15] was the chosen method because numerical boundary conditions are not required to obtain a solution. The solution of the system in Eq. (5) can be written in terms of the matrix exponential $[e^{Ax}]$ as

$$\{u\} = [e^{Ax}]\{C\} \tag{11}$$

The matrix exponential can be expressed as the infinite series [15]

$$[e^{Ax}] = \sum_{k=0}^{\infty} \frac{x^k}{k!}[A]^k \tag{12}$$

To get faster convergence, a method of scaling and squaring [16] is employed, and the series is calculated up to a value of k, which yields an acceptable error ε. The error can be defined many ways, but the current study defined the error as the difference between the one-norms of $[e^{Ax}]$ for $k-1$ and k. The value of the acceptable error was set at $\varepsilon = 0.0001$. The next step is to solve for the vector of constants $\{C\}$, using the boundary conditions. This is where the analytical formulation is discretized and the displacements are obtained in terms of the nodal displacements, as defined in Fig. 5. Applying prescribed displacements to the joined nodes on the left gives the following system of equations:

$$[BC]\{u(0)\} = \{q_{x=0}\} \tag{13}$$

in which $\{u(0)\}$ is $\{u\}$ from Eq. (6) evaluated at $x = 0$, $\{q_{x=0}\}$ is a vector containing nodal displacements q_1–q_6 as defined in Fig. 5, and the diagonal block matrix

$$[BC] = \begin{bmatrix} [bc] & 0 \\ 0 & [bc] \end{bmatrix} \tag{14}$$

with

$$[bc] = \begin{bmatrix} 1 & 0 & 0 & 0 & 0 & 0 \\ 0 & 0 & 1 & 0 & 0 & 0 \\ 0 & 0 & 0 & 1 & 0 & 0 \end{bmatrix} \tag{15}$$

Using the solution for the centerline displacements found in Eq. (11), the boundary conditions at the left side of the element [Eq. (13)] can be rewritten as

$$[BC][e^{A0}]\{C\} = \{q_{x=0}\} \tag{16}$$

in which $[e^{A0}]$ is $[e^{Ax}]$ evaluated at $x = 0$. Performing the same operation at $x = 0$ gives the second set of boundary conditions:

$$[BC][e^{Al}]\{C\} = \{q_{x=l}\} \tag{17}$$

By combining these two equations, one can find the vector of constants $\{C\}$ in terms of the nodal displacements $\{q\}$ in the following equation:

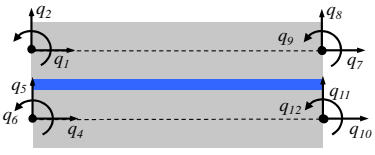

Fig. 5 Boundary conditions for a joint element: prescribed nodal displacements at $x = 0$ and $x = l$.

$$\{C\} = [z]^{-1}\{q\} \tag{18}$$

in which

$$[z] = \begin{bmatrix} [BC] & 0 \\ 0 & [BC] \end{bmatrix} \begin{bmatrix} [e^{A0}] \\ [e^{Al}] \end{bmatrix} \tag{19}$$

and $\{q\}$ is a vector containing nodal displacements q_1–q_{12} as defined in Fig. 5. This relation can be inserted into Eq. (11) to get the adherend centerline displacements in terms of the nodal degrees of freedom, $q_{1\text{–}12}$:

$$\{u\} = [N]\{q\} \tag{20}$$

in which the shape functions $[N]$ are defined as

$$[N] = [e^{Ax}][z]^{-1} \tag{21}$$

B. Define Adhesive Stress/Strain Relation

With the shape functions determined for a joint with a linear adhesive, the nonlinear constitutive stress–strain relations of the adhesive need to be defined. This can be based on measured stress–strain relations or inferred stress–strain relations from fracture properties. A stress–strain relationship based on a measured tensile stress–strain curve can be fitted with a fitting function. An inferred stress–strain relation that uses fracture properties would use a function that has its maximum stress at the mode 1 critical stress (σ_{Ic}), and the area under the curve would correspond to the critical strain energy release rate of the adhesive (G_{IC}). Regardless of the method used to define the relation, the adhesive stress σ_{az} can be written as a function of the adhesive strain ε_{az}:

$$\sigma_{az} = g(\varepsilon_{az}) \tag{22}$$

Although this paper refers to the normal stress and strain in the adhesive only, the same derivation holds for the shear strain–stress relation. It should also be noted that this stress–strain relation assumes no permanent plasticity but resembles nonlinear elasticity. Because the failing adhesive domain is eliminated in the iteration process (to be described later), the assumption of a nonlinear elastic type stress–strain law suffices for this modeling process because regions of "unloading" are minimal.

Often, the function from Eq. (22) is defined based on bulk adhesive experimental data. However, the tensile loading of a thin adhesive layer with relatively large in-plane dimensions differs greatly than that of a solid cylindrical specimen, because the adhesive layer is extremely thin in one direction and constrained from lateral displacement by the top and bottom adherends. Because of these conditions, the adhesive is effectively a body in-plane strain in the two directions perpendicular to the adhesive thickness (Fig. 6). The adhesive is constrained from contracting (Poisson's effect) in the x and y-directions while being loaded in the z-direction, which induces a stress in all three directions, commonly called a state of triaxial stress [17]. To find the stress–strain relation for a material under triaxial stress, consider first an isotropic, linearly elastic material. The normal stress in the z-direction is

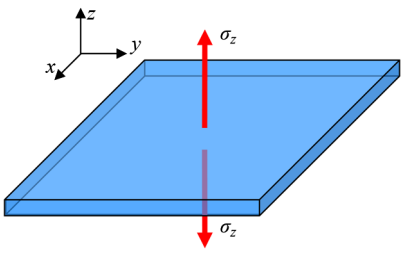

Fig. 6 A thin adhesive layer with an applied stress is in a state of triaxial stress.

$$\sigma_{az} = \frac{E_a}{1+\nu_a}\left(\varepsilon_{az} + \frac{\nu_a}{1-2\nu_a}(\varepsilon_{az} + \varepsilon_{ax} + \varepsilon_{ay})\right) \tag{23}$$

The adhesive can be assumed to be in a state of plane stress in the xy-plane, and the strains ε_{ax} and ε_{ay} can be set to zero. Then, the normal stress in the z-direction reduces to

$$\sigma_{az} = \frac{1-\nu_a}{(1+\nu_a)(1-2\nu_a)} E_a \varepsilon_{az} \tag{24}$$

This shows that the effective "resistance" to deformation in the z-direction is amplified by a factor that depends on Poisson's ratio. Although this relation is intended for linear elasticity, the relation was assumed to hold for the nonlinear stress–strain relation as well. Therefore, the stress–strain relation was redefined as

$$\sigma_{az} = \frac{1-\nu_a}{(1+\nu_a)(1-2\nu_a)} g(\varepsilon_{az}) \tag{25}$$

which effectively increases the adhesive modulus.

C. Linearize Stress/Strain Relation

To simplify calculations and avoid the need for a nonlinear solver, the loading is broken up into increments, and the stress–strain relation of the adhesive is linearized about the previous strain increment. The Taylor series expansion of the stress at the $(n+1)$th increment, can be written in terms of the strain at load step n, ε^n as

$$\sigma(\varepsilon^{n+1}) = g(\varepsilon^n) + \frac{\mathrm{d}g(\varepsilon^n)}{\mathrm{d}\varepsilon}\Delta\varepsilon + \mathrm{HOT} \tag{26}$$

in which HOT represents higher-order terms, $\Delta\varepsilon = \varepsilon^{n+1} - \varepsilon^n$, and the subscript az has been dropped from the stress and strain symbols. To linearize, the higher-order terms are ignored.

D. Calculate Adhesive Strain Energy

The adhesive normal strain energy U^{n+1} at the next load step, $n+1$, is found as the strain energy from the previous increment plus the integral of the stress as a function of strain from the previous increments to the current increment:

$$U^{n+1} = \int_{V_a}\int_{\varepsilon^n}^{\varepsilon^{n+1}} \sigma(\varepsilon)\,\mathrm{d}\varepsilon\,\mathrm{d}V + U^n \tag{27}$$

Carrying out the inner integral gives

$$U^{n+1} = \int_{V_a}\left(\frac{1}{2}\frac{\mathrm{d}g(\varepsilon^n)}{\mathrm{d}\varepsilon}(\varepsilon^{n+1})^2 + \left(g(\varepsilon^n) - \frac{\mathrm{d}g(\varepsilon^n)}{\mathrm{d}\varepsilon}\varepsilon^n\right)\varepsilon^{n+1} - g(\varepsilon^n)\varepsilon^n - \frac{1}{2}\frac{\mathrm{d}g(\varepsilon^n)}{\mathrm{d}\varepsilon}(\varepsilon^n)^2\right)\mathrm{d}V + U^n \tag{28}$$

E. Perform Rayleigh–Ritz Using Linear Adhesive Shape Functions

To obtain the stiffness and force matrices for the joint, the shape functions derived for the linear adhesive case [Eq. (5)] are used. Using Eqs. (2) and (4) and the shape functions derived for the linear adhesive case [Eq. (21)], the strain in the adhesive is found in terms of the nodal displacements, $q_{1\text{–}12}$. The strain in the adhesive at the current, $n+1$, increment is written as a function of x and $q_{1\text{–}12}$:

$$\varepsilon^{n+1} = f(q_{1\text{–}12}) \tag{29}$$

whereas the displacements from the previous increment are used to define the adhesive strain at the previous increment ε^n, as a function of x only. The energy is then minimized, which yields the ith, jth component k_{ij} of the contribution to local joint stiffness matrix from the adhesive normal strain:

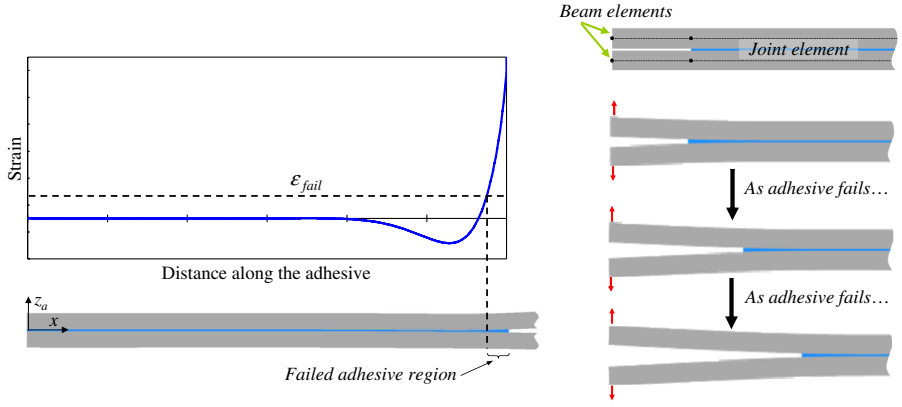

Fig. 7 Once a region of adhesive exceeds the a) failure strain, this region is considered failed and b) the joint element is shortened, whereas the adjacent beam elements are lengthened (DCB geometry depicted).

$$k_{i,j} = \frac{\partial^2}{\partial q_i \partial q_j} \int_{v_a} \frac{1}{2} \frac{\mathrm{d}g(\varepsilon^n)}{\mathrm{d}\varepsilon} (\varepsilon^{n+1})^2 \, \mathrm{d}V \tag{30}$$

and the ith component contribution of the adhesive normal strain to the local joint force vector f_i to be

$$f_i = \frac{\partial}{\partial q_i} \int_{v_a} \left(\frac{\mathrm{d}g(\varepsilon^n)}{\mathrm{d}\varepsilon} \varepsilon^n - g(\varepsilon^n) \right) \varepsilon^{n+1} \, \mathrm{d}V \tag{31}$$

Using the same steps, a similar relation can be derived for the adhesive shear strain. The contribution of the adhesive normal and shear strains to the local force vector and stiffness matrix can be added to the contributions of the two adherends. Because only the adhesive is modeled as nonlinear, the contributions of the adherends to the stiffness matrix are the same as in the linear case. The local stiffness matrix and local force vector can be used to find the local nodal displacements $\{q\}$:

$$[k]\{q\} = \{f\} \tag{32}$$

F. Assemble Global Matrices, Apply Loading, and Solve Global Equations

Once the joint element stiffness matrix and load vector are found, they are assembled with the rest of the elements in the model. The loading increment is applied, and the system of linear equations is solved at each increment. For this particular study, an in-house finite element code was used to assemble and solve the finite element global equations. Future work will implement the method into an Abaqus [13] user element to be integrated in global, vehicle-scale models.

G. Check for Adhesive Failure

Once the nodal displacements are found, Eqs. (2a) and (2b) are used to find the strain in the adhesive as a function of horizontal position x. Then, a strain-based failure criterion based on the failure strain $\{\varepsilon_{\text{fail}}\}$ is used to determine if and how much the adhesive has failed (Fig. 7a).

If failure is detected, the joint element is shortened by the length of the failed adhesive region, and the adjacent beam elements are lengthened to compensate (Fig. 7b) with no continuity of displacements imposed between them. After this step is completed, the steps described in Secs. II.A–II.G are repeated until the joint reaches equilibrium. After equilibrium is reached and further failure no longer occurs, the load is increased by one increment, and the process is repeated. Through this method, the stresses, strains, loads, and displacements for the joint can be found at each load increment as the joint deforms nonlinearly and fails progressively.

III. Results

Two different joint types were modeled with the joint element, to show some of its the capabilities and compare it with more traditional finite element models and experiments. First, a single lap joint was modeled to show the convergence of the joint element. Second, double cantilever beam (DCB) specimens, tested by Song and Waas [18], were modeled with the joint element to validate the element with another finite element model and experimental data. The specimens were loaded and unloaded several times, which is the ideal situation to see the effects of assuming nonlinear elastic adhesive, rather than elastic–plastic. Third, two additional DCB configurations were compared; one with a brittle adhesive and the other a much more

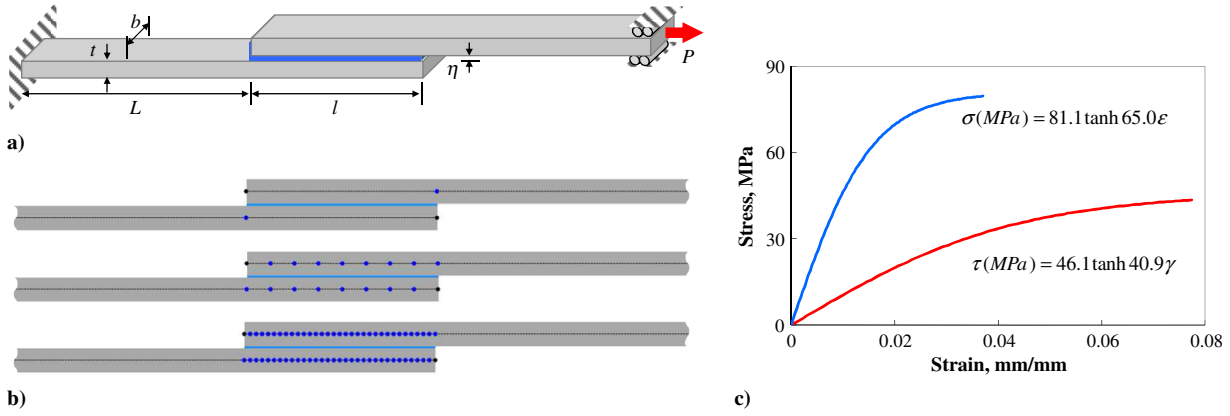

Fig. 8 Single lap joint: a) geometric parameters; b) joint element representations with one, eight, and 32 joint elements across the overlap region; and c) curve-fit of bulk tensile stress–strain response for ESP105 adhesive [19], along with an approximated shear response.

Table 1 Material properties and geometric parameters for Song and Waas [18] DCB specimens

	Adhesive		Adherend	Geometric parameters				
Specimen	E_a, GPa	G_{Ic}, N/m	E, GPa	l, mm	a, mm	b, mm	t, mm	η, μm
E7T1/G40	4.1	335	116	200	52.6	15.5	4.65	35
E719/IM7	3.3	1130	135	200	35.5	15.1	3.23	6

ductile adhesive. These tests showed how bulk adhesive properties could be used to predict the failure in a bonded joint.

A. Single Lap Joint Example

An example configuration of a single lap joint was modeled with the joint element, to show convergence with the joint element. Convergence can be an issue, because the shape functions used for the joint element came from the linearly elastic adhesive case. Once significant softening of the adhesive occurs, the shape functions are no longer exact for the problem. Because this method was created to allow a joint to be modeled with a single element, it is important to determine how much of an effect using the linearly elastic adhesive shape functions has on the stress and failure of a joint.

The configuration, along with the loading and boundary conditions, is found in Fig. 8a. The joint overlap was modeled using one element, eight elements, and 32 elements in the overlap region (Fig. 8b). The adherends were made of aluminum, and the material and geometric parameters defined in Fig. 8a are as follows: 1) adherend: $E = 70$ GPa and $\upsilon = 0.33$; and 2) geometric parameters: $l = 12.7$ mm, $L = 63.5$ mm, $b = 24.1$ mm, $t = 1.6$ mm, and $\eta = 0.125$ mm. The stress–strain behavior of the adhesive was based on the bulk adhesive tensile data of ESP105 epoxy, as reported by Harris and Adams [19] (Fig. 8c). The tensile response was modeled by fitting a tanh function to the aforementioned data. This function was chosen because it resembled the form of the response, and it gives the same response for compression and tension.

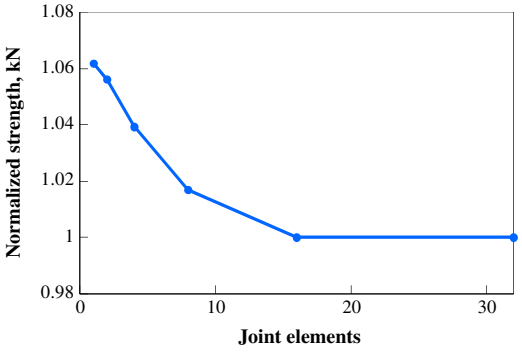

Fig. 9 Convergence of joint strength for the single lap joint with increasing joint elements.

The shear response was not obtained experimentally but rather assumed based on the tensile response. First, Poisson's ratio was taken to be 0.34, and the shear modulus was obtained based on the initial slope of the tensile curve and Hooke's law. The maximum stress of the shear response was found by assuming that the adhesive behaves according to J2 flow theory and that this holds true after initial yield. The shear failure strain was calculated by assuming that the strain energy at failure was the same for shear and tensile loading. The shear and tensile responses of the adhesive were kept uncoupled, and adhesive failure was initiated when either the shear or normal strain reached the corresponding failure value.

The difference in joint strength predictions between models with one, eight, and 32 joint elements is illustrated in Fig. 9. Using one element still gives a reasonable answer, and more than two elements are needed to get within 5% of the converged strength. The shear and peel stress in the adhesive layer at a load of 5.2 kN for one, eight, and 32 elements are shown in Fig. 10. The peel stresses are almost identical for all cases, mainly due to the fact that less softening has occurred in the z-direction. There is a larger difference in shear stress between the models with one, eight, and 32 elements, because the adhesive has softened more in shear. This discrepancy can be explained by looking at the tangential modulus shown in Fig. 11. The adhesive has softened significantly at the ends, making the tangential modulus a function of x. The shape functions were found for a constant modulus adhesive, which no longer represents the softened adhesive. Therefore, the shape functions do not represent the exact solution after softening has occurred. To improve the solution, the shape functions would have to be calculated at each load increment based on the tangential modulus at the previous increment. In this way, the joint could be modeled with one element without a loss in accuracy.

A major source of error for this type of joint is the fact that large displacements and rotations were not taken into account in the joint element formulation. The joint already had rotations in excess of 1° at 13% of the maximum load, making this problem highly nonlinear with respect to geometry. Harris and Adams [19] reported this joint to have a strength of 9.9 ± 0.65 kN, whereas the joint element model predicted a joint strength of 5.8 kN. This illustrates the need to include large rotations when modeling single lap joints, making it imperative that geometric nonlinearities be included to model the strength of single lap joints. This capability will be included in future versions of the model.

As a side note, it has been observed that adhesive softening is responsible for the spreading of the stress in the joint in a more even manner [8,19]. The adhesive properties become naturally graded

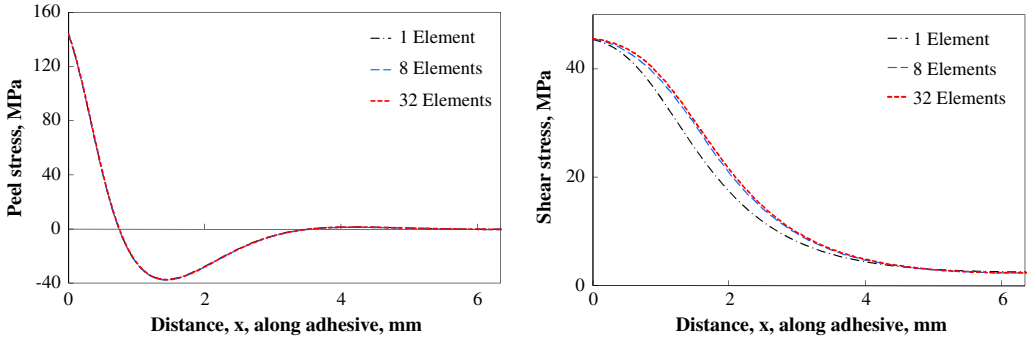

Fig. 10 Convergence study for the joint element modeling a single lap joint with ESP105 adhesive: a) adhesive peel stress and b) adhesive shear stress using one, eight, and 32 elements to model the joint overlap.

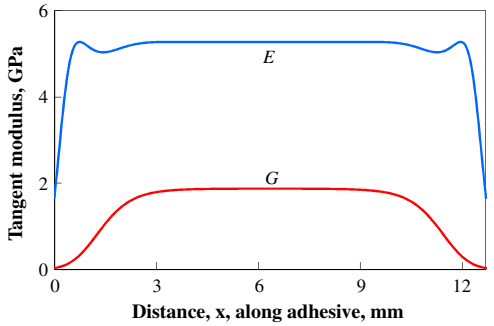

Fig. 11 Tangent shear and normal modulus of single lap joint before failure.

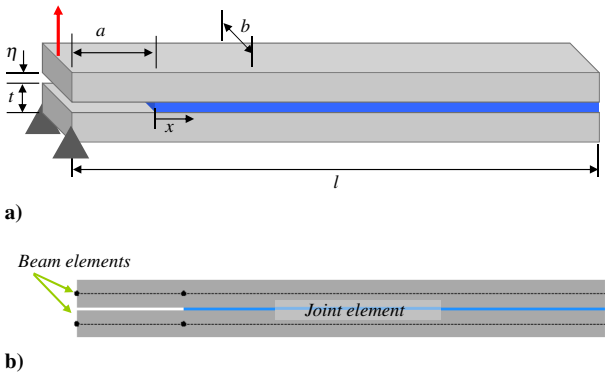

Fig. 12 A typical DCB specimen: a) the geometric parameters and boundary conditions for the DCB specimens and b) the mesh for the joint element DCB model.

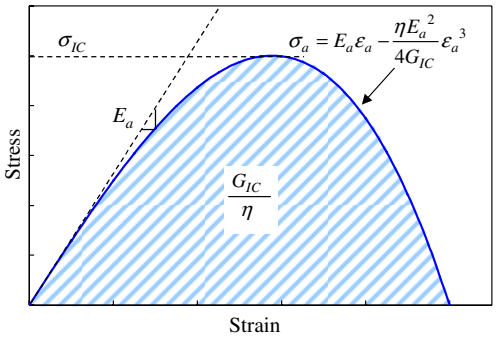

Fig. 13 The stress–strain relation of the adhesive was defined based on the mode 1 energy release rate and modulus.

along the joint to minimize the stress concentration. The same effect could be achieved by artificially grading the adhesive along the length of the adhesive. Such a grading could decrease the maximum stress of the joint without incurring any damage of the adhesive.

B. Comparison with Published Double Cantilever Beam Results

The ability of the joint element to predict the force vs displacement behavior was assessed through comparison with experimental and finite element results published by Song and Waas [18]. The DCB test is more suited for experimental validation rather than a single lap joint, for several reasons. First, the effects of geometric nonlinearity are often much smaller. Second, the stable progressive failure exhibited in DCB specimens shows the capability of the joint element to fail progressively. Most single lap joints exhibit no stable crack growth; the crack grows almost instantaneously after crack initiation. Therefore, the DCB example illustrates the full capability of the joint element to grow a crack progressively. This particular dataset was chosen because the authors stated that the failure was fully interlaminar and cohesive, which is the type of failure currently modeled by the joint element.

Figure 12 shows a DCB specimen and the geometric parameters. The DCB specimens were constructed from two different 48-ply unidirectional composite laminates, E719/IM7 and E7T1/G40. The adhesive was one of the interlaminar matrix layers. The nonlinear stress–strain relation of the adhesive was based on G_{IC} and E_a (Fig. 13), as was done by Song and Waas [18]. Normally, the mode 1 critical stress is preferred rather than the modulus, but this value was not provided by the authors. The geometric and material properties of the specimens are shown in Table 1. During the test, the loading was halted and the specimen was unloaded several times to measure the crack length within the specimen. The DCB specimen was modeled using one joint finite element accompanied by two beam elements on the top and bottom of the joint, as shown in Fig. 12b.

Figure 14a compares the experimental force/displacement responses for the E719/IM7 DCB specimen acquired by Song and Waas [18], along with the response predicted by the present joint element model. As can be seen, the present model was quite accurate at predicting the progressive failure of the joint based on the given material properties and parameters. The behavior of the E7T1/G40 DCB specimens, shown in Fig. 14b, was not predicted as accurately by the joint element model. The joint element model predicted a stiffer elastic response and higher peak load, but the subsequent response is captured quite well. This comparison shows that the joint element can be used with fracture properties similar to discrete cohesive zone models in predicting the behavior of DCB joints.

Although these two DCB specimens were both loaded and unloaded several times, the nonlinear elastic material model used for the joint element adhesive was still sufficient to capture the overall behavior. This is because the stress concentration at the end of the joint causes the plastic zone in the adhesive to remain small. Therefore, the advantage of modeling the adhesive as elastic–plastic over nonlinear elastic is not great enough to justify the extra effort and complication. As long as the failure incurred due to crack growth is accounted for, the global response will be reasonably represented.

C. Comparison with Experimental Results for Aluminum Double Cantilever Beam Specimens

DCB specimens were manufactured and tested to compare two paste adhesives, EA 9394 and EA 9309.3NA. The results of these tests were used to assess the ability of the joint finite element to predict the difference in performance of two adhesives with very different stress–strain relations, based on material properties obtained from tensile tests. Solid cylindrical specimens with a 3.175 mm diameter and 3.175-mm-long test section were machined out of cast adhesive cylinders. The specimens were tested at NASA John H. Glenn Research Center at Lewis Field, and digital image correlation (DIC) techniques (Fig. 15a) were used to obtain the axial strain of the specimen at different loads. The strains for several points in the gauge section were averaged, and the stress was found by assuming constant stress in the cross section. Figure 15b shows characteristic stress–strain data for the two adhesives and the

Table 2 Material properties and geometric parameters of DCB specimens

	Adhesive				Adherend	Geometric parameters				
Specimen	E_a, GPa	σ_u, MPa	$\varepsilon_{\text{fail}}$	υ	E, GPa	l, mm	a, mm	b, mm	t, mm	η, mm
EA 9394	4.2	49.6	0.016	0.4	69	152.4	63.5	25.4	12.7	0.6
EA 9309.3NA	2.7	41.3	0.068	0.42	69	152.4	63.5	25.4	12.7	0.55

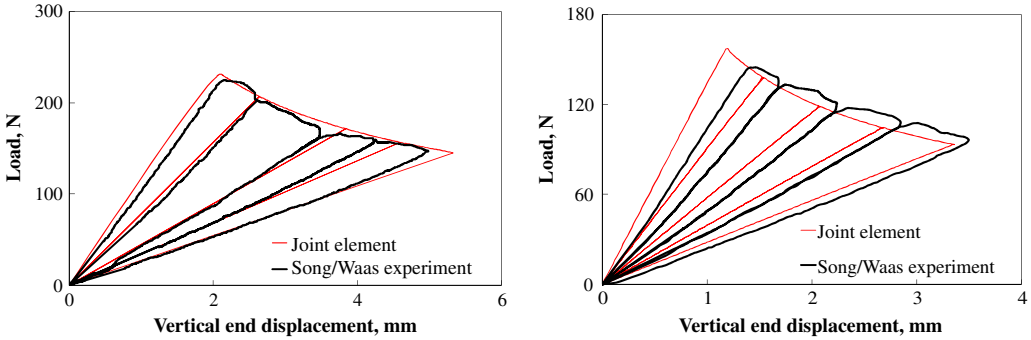

Fig. 14 Load vs displacement curves for a) E719/IM7 and b) E7T1/G40 DCB specimens tested by Song and Waas [18], along with the present joint element model.

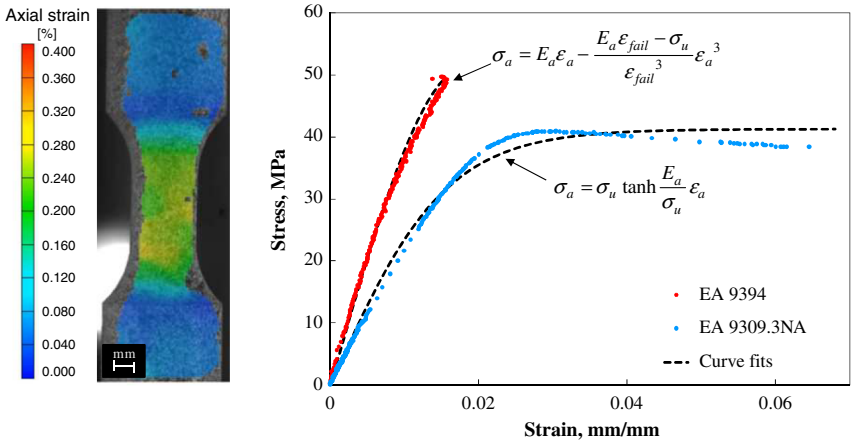

Fig. 15 Using a) cylindrical tensile specimens and DIC, the b) stress–strain relations of the adhesives EA 9394 and EA 9309.3NA could be defined by curve-fitting experimental data.

Fig. 16 Two adherends of an EA 9394 DCB specimen after complete failure. Adhesive found on both adherends indicates that failure occurred within the adhesive layer as desired.

equations used to fit the data with a curve. The material parameters used in the equations are found in Table 2. The functions were chosen because they result in the same curve in compression and tension and seem to fit the data adequately.

Because the joint element considers only failure in the adhesive (cohesive failure), care was taken to ensure that the interface between the adherends and adhesive of the DCB specimens would not fail. The adherends were 7071 T6 aluminum, and the surfaces to be bonded were sanded, etched in lye, and anodized in a sulfuric acid solution before bonding [20]. This treatment was sufficient to produce failures in the adhesive layer, as can be seen on the failure surfaces of a postmortem specimen in Fig. 16. The failed specimen has adhesive covering both adherends, which means that the interface was not the plane of failure. Glass beads were used to maintain a consistent bond line thickness throughout the specimen, and pressure was applied to the specimen during curing. The specimens were allowed to cure for seven days at room temperature.

Three DCB specimens for each adhesive were tested on an Instron machine at 0.5 mm/ min. All specimens failed cohesively, like the specimen in Fig. 16. The force/displacement curves for all six specimens are shown in Fig. 17. The high strain-to-failure of EA 9309.3NA caused these specimens to hold over two times the load of EA 9394 specimens. The EA 9309.3NA specimens held so much load that the aluminum adherends deformed plastically before the adhesive failed. This can be seen in the plot as a gradual rounding before a drop in load. The EA 9394 specimens exhibited a load plateau rather than dropping in load after adhesive failure was initiated. It is possible that air bubbles in the adhesive caused the adhesive to fail prematurely, allowing the joint to not drop in load carrying capacity after failure initiated.

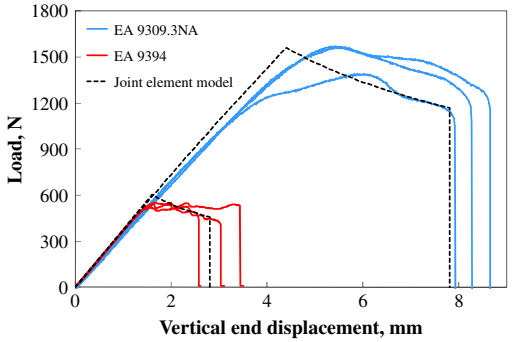

Fig. 17 Load vs displacement curves for DCB specimens with aluminum adherends and EA 9394 and EA 9309.3NA adhesive, along with the joint finite element model prediction.

The joint element model was able to capture the behavior of the joints rather well. It was found that compliance in the experimental load train caused the models to overpredict even the initial linear portion of the loading. To compensate for this system compliance, the length of the adherends was increased by 7.5% for both DCB specimen types. This number was determined by fitting a linearly elastic model to the initial portion of the experimental force/displacement plot. Although not exactly matching the experimental data, the model was rather accurate, considering the aforementioned adherend plasticity and air bubbles in the end of the adhesive. These experiments were very effective in displaying the ability of the joint element to predict failure, along with showing how constitutive relations can be applied to get progressive failure of a thin adhesive layer.

IV. Conclusions

This study showed how a bonded joint finite element could be used to capture the behavior of an entire joint, by using an analytical method to solve for the appropriate shape functions rather than prescribe the shape functions using a polynomial interpolation. This joint element is intended for use as a design tool that can model a joint in a mesh-independent manner and still couple with global vehicle-scale finite element models. As a design tool, it is not intended to replace high-fidelity detailed models, but enable fast, efficient sizing and design of bonded joints. Some of the limitations of this model are contained in the assumptions used to generate the shape functions. First, the adhesive is modeled as a bed of springs rather than a continuum, and so the traction-free surface of the adhesive is not represented in the joint element. Additionally, the adherends are assumed to behave like beams or wide plates under cylindrical bending. Thus, variations in fields through the width of the joint are not captured. Future work will include constructing a three-dimensional plate or shell element that can be used when effects through the width need to be captured.

Additionally, progressive failure was included in the model by defining the stress as a nonlinear function of the strain and enforcing an uncoupled strain-based failure criterion. Progressive failure of the adhesive was approximated, by shortening the joint element by the length of the failed adhesive and lengthening the adjoining beam elements. The shape functions obtained for a joint with a linearly elastic adhesive were used for the nonlinear adhesive case. Softening of the adhesive as the stress increases causes the shape functions to no longer be exact. However, a mesh convergence study conducted for a single lap joint configuration showed that the difference in strength predictions between using one joint element and 32 were only approximately 6%. The predicted strength for a single lap joint did not match well with an experimental result from the literature, most likely because of a lack of large rotation inclusion in the joint element, which will be added in future versions of the element. Additionally, it was shown how softening of the adhesive layer where the stress is the highest causes the adhesive to spread the stress more evenly across the joint. Such an effect could be replicated without adhesive softening by artificially grading the modulus of the adhesive across the joint.

The accuracy of the joint element model was assessed through comparison with experimental DCB test results published by Song and Waas [18]. Results showed that the joint element model could capture the force/displacement behavior of the joint quite well, with a significant computational efficiency advantage compared with a traditional finite element analysis. Two of the DCB specimens were repeatedly loaded and unloaded. Although the joint element contains a nonlinear elastic adhesive, the concentrated plastic zone often found in joints caused the effect to be minimal. A further comparison was made with DCB specimens created and tested by the authors. The adhesive was characterized with a bulk adhesive tensile test, and results showed good correlation.

These DCB comparisons also demonstrated how the stress–strain relation of the adhesive could be obtained from bulk tensile tests or inferred from fracture parameters (fracture toughness and cohesive strength). When using tensile test results for the adhesive stress–strain relation, stress triaxiality was used to modify the effective one-dimensional stress–strain relation. With proper implementation of this method, a single finite element can be used in a broader, global-scale model to capture the approximate behavior and failure of joints. The joint element allows efficient parametric studies to take place within the framework of a global-scale structural finite element model, allowing more efficient and thorough design of adhesively bonded joints.

Acknowledgments

Portions of this work were financially supported by the Space Vehicle Technology Institute, under grant NCC3-989, jointly funded by NASA and the Department of Defense. Additional financial support was provided by NASA John H. Glenn Research Center at Lewis Field, through the Graduate Student Research Program Fellowship. The authors would like to thank Justin Bail of the Ohio Aerospace Institute, for testing the adhesive tensile specimens at NASA John H. Glenn Research Center at Lewis Field.

References

[1] Hart-Smith, L., "Adhesive Bonding of Composite Structures: Progress to Date and Some Remaining Challenges," *Journal of Composites Technology and Research*, Vol. 24, No. 3, 2002, pp. 133–151. doi:10.1520/CTR10566J

[2] Frostig, Y., Thomsen, O., and Mortensen, F., "Analysis of Adhesive-Bonded Joints, SquareEnd, and Spew-Fillet- High-Order Theory Approach," *Journal of Engineering Mechanics*, Vol. 125, No. 11, 1999, pp. 1298–1307. doi:10.1061/(ASCE)0733-9399(1999)125:11(1298)

[3] Gustafson, P. A., and Waas, T. A., "A Macroscopic Finite Element for a Symmetric Double-Lap Joint Subjected to Mechanical and Thermal Loading," AIAA/ASME/ASCE/AHS/ASC 48th SDM Conference, AIAA Paper 2007-2308, Honolulu, HI, 23–26 April 2007.

[4] Volkersen, O., "Die Nietkraftverteilung in Zugbeanspruchten mit Konstanten Laschenquerschritten," *Luftfahrtforschung*, Vol. 15, 1938, pp. 41–47.

[5] Goland, M., and Reissner, E., "The Stresses in Cemented Joints," *Journal of Applied Mechanics*, Vol. 11, No. 1, 1944, pp. A17–A27.

[6] Ojalvo, I. U., and Eidinoff, H. L., "Bond Thickness Effects upon Stresses in Single Lap Adhesive Joints," *AIAA Journal*, Vol. 16, No. 3, 1978, pp. 204–211. doi:10.2514/3.60878

[7] Hart-Smith, L. J., "Adhesive Bonded Single Lap Joints," NASA CR 112236, Douglas Aircraft, McDonnel Douglas Corp., Long Beach, CA, 1973.

[8] Mortensen, F., and Thomsen, O. T., "Analysis of Adhesive Bonded Joints: A Unified Approach," *Composites Science and Technology*, Vol. 62, Nos. 7–8, 2002, pp. 1011–1031. doi:10.1016/S0266-3538(02)00030-1

[9] Zhang, J., Bednarcyk, B. A., Collier, C., Yarrington, P., Bansal, Y., and Pindera, M. J., "Analysis Tools for Adhesively Bonded Composite Joints Part 2: Unified Analytical Theory," *AIAA Journal*, Vol. 44, No. 8, 2006, pp. 1709–1719. doi:10.2514/1.15664

[10] Delale, F., Erdogan, F., and Aydinoglu, M. N., "Stresses in Adhesively Bonded Joints: A Closed-Form Solution,"*Journal of Composite Materials*, Vol. 15, No. 3, 1981, pp. 249–271. doi:10.1177/002199838101500305

[11] Zhang, J., Bednarcyk, B. A., Collier, C., Yarrington, P., Bansal, Y., and Pindera, M. J., "3D Stress Analysis of Adhesively Bonded Composite Joints," AIAA/ASME/ASCE/AHS/ASC 46th SDMConference, AIAA Paper 2005-2021, Austin, TX, 18–21 April 2005.

[12] Stapleton, S. E., and Waas, A. M., "Macroscopic Finite Element for a Single Lap Joint," AIAA/ASME/ASCE/AHS/ASC 50th SDM Conference, AIAA Paper 2009-2449, Palm Springs, CA, 4–7 May 2009.

[13] ABAQUS, Inc., ABAQUS User Manual, Ver. 6.7-1 [Electronic Resource], 2006.

[14] Tsai, M. Y., and Morton, J., "An Evaluation of Analytical and Numerical Solutions to the Single-Lap Joint," *International Journal of Solids and Structures*, Vol. 31, No. 18, 1994, pp. 2537–2563. doi:10.1016/0020-7683(94)90036-1

[15] Chen, C., *Linear System Theory and Design*, 3rd ed., Oxford Univ. Press, New York, 1999, p. 68.

[16] Molder, C., and Van Loan, C., "Nineteen Dubious Ways to Compute the Exponential of a Matrix, Twenty-Five Years Later," *SIAM Review*, Vol. 45, No. 1, 2003, pp. 3–49.

[17] Wang, C. H., and Rose, L. R. F., "Determination of Triaxial Stresses in Bonded Joints," *International Journal of Adhesion and Adhesives*, Vol. 17, No. 1, 1997, pp. 17–25. doi:10.1016/S0143-7496(96)00028-0

[18] Song, S. J., and Waas, A. M., "Mode 1 Failure of Laminated Polymeric Composites," *Engineering Fracture Mechanics*, Vol. 49, No. 1, 1994, pp. 17–27. doi:10.1016/0013-7944(94)90107-4

[19] Harris, J. A., and Adams, R. D., "Strength Prediction of Bonded Single Lap Joints by Non-Linear Finite Element Methods," *International Journal of Adhesion and Adhesives*, Vol. 4, No. 2, 1984, pp. 65–78. doi:10.1016/0143-7496(84)90103-9

[20] Burst, N., and Adams, D. O., "Investigating the Thin-Film Versus Bulk Material Properties of Structural Adhesives," U.S. Department of Transportation/Federal Aviation Administration AR-06/45, May 2008.

N. Wereley
Associate Editor